

Renjian Li* and Ming Li

Horn Point Lab
University of Maryland Center for Environmental Science
P.O. BOX 775
Cambridge, MD 21613, U.S.A.

Submitted to Journal of Physical Oceanography

1

Early Online Release: This preliminary version has been accepted for publication in *Journal of Physical Oceanography* cited, and has been assigned DOI 10.1175/JPO-D-21-0261.1. The final typeset copyedited article will replace the EOR at the above DOI when it is published.

^{*} Corresponding author: Renjian Li, Horn Point Lab., University of Maryland Center for Environmental Science, 2020 Horns Point Road, Cambridge, MD 21613, U.S.A. Email: rli@umces.edu.

ABSTRACT

Using an idealized channel representative of a coastal plain estuary, we conducted numerical simulations to investigate the generation of internal lee waves by lateral circulation. It is shown that the lee waves can be generated across all salinity regimes in an estuary. Since the lateral currents are usually subcritical with respect to the lowest mode, mode-2 lee waves are most prevalent but a hydraulic jump may develop during the transition to subcritical flows in the deep channel, producing high energy dissipation and strong mixing. Unlike flows over a sill, stratified water in the deep channel may become stagnant such that a mode-1 depression wave can form higher up in the water column. With the lee wave Froude number above 1 and the intrinsic wave frequency between the inertial and buoyancy frequency, the lee waves generated in coastal plain estuaries are nonlinear waves with the wave amplitude scaling approximately with V/\overline{N} where V is the maximum lateral flow velocity and \overline{N} is the buoyancy frequency. The model results are summarized using the estuarine classification diagram based on the freshwater Froude number Fr_f and the mixing parameter M. Δh decreases with increasing Fr_f as stronger stratification suppresses waves, and no internal waves are generated at large Fr_f . Δh initially increases with increasing M as the lateral flows become stronger with stronger tidal currents, but decreases or saturates to a certain amplitude as M further increases. This modeling study suggests that lee waves can be generated over a wide range of estuarine conditions.

1 Introduction

Nonlinear internal waves are widely observed in the stratified coastal ocean and play an important role in generating turbulent mixing and transporting biochemically important materials. The conversion of barotropic tidal energy to internal waves is now generally accepted as a major source for mixing in the ocean (Munk and Wunsch 1998). In contrast, internal waves in estuaries have not attracted much attention (Wang 2006), except for flows over sills at the entrance to deep fjords (e.g. Farmer and Armi 1999; Cummins et al. 2003; Gregg and Pratt 2010) and in deep estuaries (e.g. Bourgault and Kelley 2003; Bourgault et al. 2007; Richards et al. 2013). In shallow coastal plain estuaries, turbulence has been mostly attributed to boundary layer turbulence (Geyer and MacCready 2014). Dissipation by bottom friction is assumed to be the dominant sink for the barotropic tidal energy, and most studies have focused on the bottom dissipation.

Several previous observations however did find internal waves in coastal plain estuaries. Echo-sounding surveys across a cross-section in a partial mixed estuary, Southampton Water, showed internal isopycnal oscillations with a wave period of 4 - 8 min (Dyer 1982). Using moored current measurements, Groeskamp et al. (2011) observed nonlinear internal solitary waves in the highly energetic Marsdiep channel. In Chesapeake Bay, early observations using thermistor chain showed high-frequency internal waves with large isotherm displacements (Sarabun and Dubbel 1990). Recent observation found that energy dissipation rate ε in the pycnocline reached 1×10^{-4} m² s⁻³ during the passage of internal solitary waves, three orders of magnitude larger than the background value (Xie et al. 2017a). Strong mixing has also been associated with the passage of internal waves in other estuaries (New et al. 1986, Sturley and Dyer 1992). For example, internal waves generated by tidal flow over a trench in the Hudson River estuary produced enhanced turbulent dissipation above the trench (Peters 1999). These observations suggest that internal waves can be another pathway to turbulent mixing in the stratified estuaries, but mechanisms for internal wave generation are not yet well understood. Neither is it known how prevalent internal waves are in coastal plain estuaries.

Based on high resolution temperature and velocity measurements at a mid-bay section of

Chesapeake Bay, Xie et al. (2017b) proposed a mechanism in which an internal lee wave is generated over the flank of the deep channel when tidally-driven lateral currents become supercritical and the lee wave subsequently propagates toward the shallow shoal, evolving into a train of solitary waves. To test the first part of this hypothesis, Xie and Li (2019) used a realistic model of Chesapeake Bay to simulate the internal lee waves observed during the field experiment and confirmed the mechanism of lee wave generation by the lateral currents. However, this study did not identify hydrodynamic conditions at which the stratified lateral flows are conducive to generating the internal lee waves. It remains unknown under what river flow and tidal current conditions that the internal lee waves could be generated in a generic coastal plain estuary.

Observations at the Knight Inlet revealed a rich variety of internal lee wave and hydraulic jump structures under different river flow and tidal conditions (Farmer and Smith 1980). Under typical summer conditions tidal flows are subcritical with respect to the lowest mode but supercritical with respect to higher modes, resulting a mode-2 lee wave or jump. When tidal flows become supercritical with respect to all modes, however, the transition from subcritical upstream flow to an accelerating supercritical downslope flow generates an internal hydraulic jump (Farmer and Armi 1999). Flow interactions with a topographic depression such as the deep channel in a coastal plain estuary could be different from flow interactions with a sill. Previous modeling studies of atmospheric flows over a valley showed flow structures such as valley-flow stagnation, lee waves, internal wave breaking, and hydraulic jumps, which are quite different from flows over a hill (Rotunno and Lehner 2016, Lehner et al. 2016). Therefore, modeling studies are needed to document possible range of internal wave and flow structures that might be produced by the interaction between the lateral flows and the valley in the deep channel. Moreover, coastal plain estuaries are much shallower than fjords and costal oceans such that bottom friction and turbulent mixing generated in the bottom boundary layer could affect the generation of the internal lee waves.

In this study an idealized straight estuarine model with channel-shoal bathymetry is used to examine the generation of internal lee waves under a range of river flows and tidal forcing conditions. The paper is structured as follows. In section 2, the model configuration and

numerical experiments are described. Section 3 presents a detailed analysis of processes and features of the lateral wave generation in a coastal plain estuary. In section 4 we explore lee waves over a range of river flows and tidal forcing conditions and interpret the wave generation in terms of internal hydraulics. The model results are summarized in a regime diagram in section 5. Concluding remarks are made in section 6.

2 Methods

2.1 Model descriptions and numerical experiments

The Regional Ocean Modeling System (ROMS) is used to configure a model for the idealized straight estuarine channel. The model domain is an estuary-shelf system (Fig. 1a), following Hetland and Geyer (2004), Cheng et al. (2010, 2011) and Li et al. (2014). The estuarine part of the model domain is a straight channel and does not have slope in the along-channel direction. The channel is 750 km long to damp out tides before they reach the upstream boundary and the width of the channel is set at 8 km. The cross-channel section has a channel-shoal bathymetry consisting of a triangular deep channel in the center and two flat shoals on each side (Fig. 1b). The shoal is 10 m deep (D = 10 m). The depth (H) of the deep channel is 10 m and the width (L) is 2 km. The continental shelf is 80 km wide and has a fixed cross-shelf slope of 0.05%. The total model domain has 240 grid cells in the east-west direction, 79 grid cells in the north-south direction, and 20 layers in the vertical direction. The estuarine channel has 200 grid cells in the along-channel direction and 41 grid cells in the cross-channel direction. The along-channel grid size increases exponentially from the estuary mouth (100 m) to its head (12 km), providing a highly resolved estuarine region. In the numerical experiments conducted, the estuary length (L_1) , defined as the distance from the estuary mouth to the upstream location where the vertically averaged salinity in the thalweg is 1 psu, is less than 300 km. The cross-channel grid in the estuary is uniformly distributed and the vertical layers are uniformly discretized.

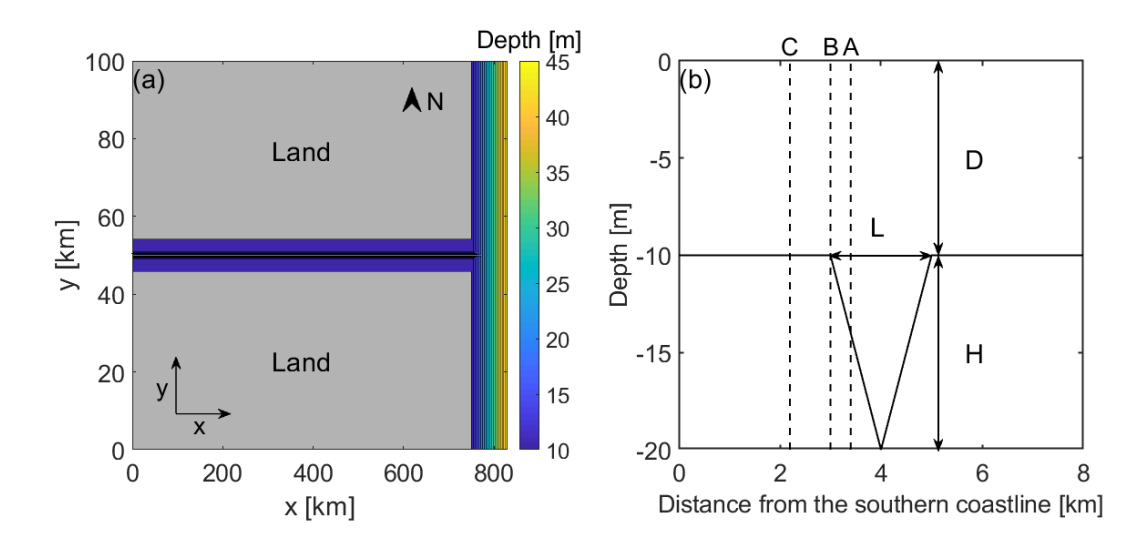


Figure 1. (a) Schematic of the numerical model domain consisting of a straight estuarine channel and a shelf. (b) Cross-channel section featuring a triangular-shaped deep channel and flat shallow shoals. The black dashed lines mark the location of site A, site B and site C (shown in Fig. 3) respectively.

The model is forced by tides at the offshore (eastern) open boundary and by river flow at the upstream (western) end of the estuarine channel. At the upstream boundary, a momentum boundary condition is imposed on the depth-averaged velocity. The inflowing river water is prescribed to have zero salinity. To simplify time series analysis, we impose a semidiurnal tide with the period of 12 h. The salinity of the coastal ocean is set at 35 psu. The open-ocean boundary is treated with a Chapman condition for surface elevation, a Flather condition for barotropic velocity, and an Orlanski-type radiation condition for baroclinic velocity and scalars (Marchesiello et al. 2001). A quadratic stress is exerted at the seabed, assuming that the bottom boundary layer is logarithmic with a roughness height of 0.5 mm. The Coriolis parameter is set at 1.0×10^{-4} rad s⁻¹.

The vertical eddy viscosity and diffusivity are computed using the k-kl turbulence closure scheme (Warner et al. 2005). In this closure scheme, the turbulent kinetic energy k and turbulent length scale l are calculated by solving two prognostic equations for k and kl. The eddy viscosity K_V and eddy diffusivity K_S are then given by

$$K_V = \sqrt{2k}lS_M + \gamma, \ K_S = \sqrt{2k}lS_N + \gamma_S, \tag{1}$$

where γ and γ_S are the background eddy viscosity and diffusivity and set at 1×10^{-5} m² s⁻¹. S_M and S_N are stability functions that describe the effects of shear and stratification (Kantha and

Clayson, 1994). The energy dissipation rate is calculated using

$$\varepsilon = \left(c_{\mu}^{0}\right)^{3} k^{\frac{3}{2}} l^{-1},\tag{2}$$

where $c_{\mu}^{0} = 0.5544$. We also conducted model runs using the k- ε and k- ω turbulence closure schemes and found almost identical results.

The model was initialized with no flow, a flat sea surface, and a uniform salinity of 35 psu. To simplify, temperature is uniform everywhere and does not change with time. Using a tidal amplitude (η_t) of 1.1 m and a sectionally averaged river flow (U_r) of 0.03 ms⁻¹, the model was run for 360 days to reach a quasi-steady state. The salinity distribution from this run was then used as the initial salinity condition in each of the following numerical experiments. Results obtained at the quasi steady state, during which tidally averaged circulation and stratification did not change with time (after 120 or so more days of integration), were used for the analysis.

A total of 24 model runs were conducted over a range of river discharges and tidal amplitudes to investigate the generation of internal lee waves by lateral circulation in the idealized estuary (Table 1).

Run	$\eta_{_t}$	M	U_r	Fr_f	L_1	$Fr_{2\text{max}}$	\overline{N}	$\overline{N}H/V$	Vk
1	0.5	0.30	0.005	0.0029	371	1.10	0.033	3.12	2.9×10 ⁻⁴
2	0.5	0.30	0.01	0.0058	310	0.68	0.048	5.68	2.0×10^{-4}
3	0.5	0.29	0.03	0.017	211	0.57	0.080	10.88	1.9×10^{-4}
4	0.5	0.26	0.05	0.029	184	0.46	0.092	15.10	1.6×10^{-4}
5	0.5	0.25	0.07	0.041	171	0.42	0.11	18.40	1.6×10^{-4}
6	0.6	0.39	0.005	0.0029	334	1.29	0.036	2.61	3.5×10^{-4}
7	0.6	0.41	0.01	0.0058	280	1.15	0.039	3.22	3.3×10^{-4}
8	0.6	0.38	0.03	0.017	191	1.00	0.071	5.48	3.6×10^{-4}
9	0.6	0.36	0.05	0.029	157	0.82	0.093	7.96	3.0×10^{-4}
10	0.6	0.37	0.07	0.041	144	0.79	0.10	8.78	3.1×10^{-4}
11	0.8	0.62	0.005	0.0029	307	1.60	0.022	1.88	4.1×10^{-4}
12	0.8	0.61	0.01	0.0058	249	1.50	0.032	2.21	4.6×10^{-4}
13	0.8	0.61	0.03	0.017	147	1.38	0.051	2.75	5.6×10 ⁻⁴
14	0.8	0.67	0.05	0.029	119	1.37	0.067	3.26	5.8×10^{-4}
15	0.8	0.72	0.07	0.041	106	1.31	0.086	4.01	5.7×10 ⁻⁴

16	1.1	0.92	0.005	0.0029	188	1.32	0.035	3.41	2.4×10 ⁻⁴
17	1.1	0.93	0.01	0.0058	163	1.46	0.033	2.06	4.4×10^{-4}
18	1.1	0.98	0.03	0.017	116	1.41	0.037	2.33	5.3×10^{-4}
19	1.1	1.27	0.05	0.029	81	1.60	0.072	3.09	6.1×10^{-4}
20	1.1	1.31	0.07	0.041	72	0.63	0.11	9.97	2.2×10^{-4}
21	1.3	1.27	0.01	0.0058	114	1.97	0.080	5.55	3.4×10^{-4}
22	1.3	1.54	0.03	0.017	80	2.24	0.10	9.83	3.0×10^{-4}
23	1.3	1.45	0.05	0.029	76	1.30	0.086	4.84	3.4×10^{-4}
24	1.3	1.69	0.07	0.041	60	2.30	0.12	10.80	4.9×10 ⁻⁴

Table 1. Summary of numerical experiments in which η_t is the tidal amplitude (m) at the open boundary, M is the estuarine mixing number, U_r is the river flow velocity (m s⁻¹), Fr_f is the freshwater Froude number, L_1 is the salt intrusion length (km), $Fr_{2\text{max}}$ is the maximum mode-2 Froude number at the left channel-shoal interface of the mid-estuary cross-section, \overline{N} is the averaged buoyancy frequency over the deep channel at the mid-estuary cross-section, $\overline{N}H/V$ is the topographic Froude number, and Vk is the intrinsic frequency for the lee waves.

2.2 Froude number analysis

To interpret the internal lee wave generation process, we calculated the Froude number

$$Fr_i = \frac{v}{c_i} \tag{3}$$

where v is the depth-averaged lateral flow velocity in the lower layer (Xie et al., 2017) and c_i is the phase speed of the ith mode of internal waves. The phase speed c_i is found by solving the following eigenvalue problem (Gill, 1982):

$$\frac{d^2\Phi(z)}{dz^2} + \frac{N^2(z)}{c_i^2}\Phi(z) = 0,$$
 (4)

with the boundary conditions $\Phi(0) = \Phi(-h) = 0$ where $\Phi(z)$ is the modal function of the vertical velocity, h is the water depth and N(z) is the buoyancy frequency. The Froude number has been widely used in previous studies of internal lee waves by flow-topography interaction (e.g. Vlasenko et al. 2013; da Silva et al. 2015).

A mode-1 lee wave can develop when $Fr_1 > 1$ and typically features a depression or elevation in isopycnals. A mode-2 lee wave can develop when $Fr_2 > 1$ and typically features a bulge in isopycnals. An internal hydraulic jump involves an abrupt isopycnal lift during a

transition from supercritical to subcritical flows.

3. Lateral wave generation

3.1 Generation and propagation of internal lee waves

We first present a detailed case study of wave generation by lateral circulation in the estuarine channel, with the tidal amplitude $\eta_t = 0.8$ m and river flow $U_r = 0.03$ m s⁻¹ (run 13 in Table 1). The estuary length (L_1), as defined by the location of vertically averaged 1 psu isohaline in the along channel section, is 147 km. The mid-estuary cross-section at $L_1/2$ is chosen to investigate the wave generation process. Figure 2a shows the time series of sectionally averaged along-channel tidal velocity and depth-averaged lateral flow velocity in the bottom layer. There is a phase lag of 2-3 hours between the peak lateral velocity and peak along-channel velocity. The lateral flows at the left channel-shoal interface reach a peak speed of 0.18 m s⁻¹ during the ebb tide.

Snapshots of lateral circulation and salinity distribution at the mid-estuary cross-section are shown in Fig. 2. A counter-clockwise lateral circulation (looking into the estuary) develops during the ebb tide (Figs. 2b-d). At the maximum ebb tide T1, no isohaline displacements appear over the deep channel and $Fr_2 < 1$ (Figs. 2b & 2e). At T2, wave perturbation of small amplitude starts to be generated over the left edge of the deep channel as the lateral flows (ν) become critical at the left channel-shoal interface (Figs. 2c & 2f). When the bottom lateral flows become supercritical at T3, a large-amplitude internal lee wave with a characteristic mode-2 bulge structure appears at this location and is arrested (Figs. 2d & 2g). Subsequently, the ebb tide subsides and the lateral currents weaken. At T4 when the lateral flows become subcritical (Fig. 2k), the lee wave propagates upward and onto the left shoal while its amplitude decreases (Fig. 2h). Meanwhile, the trailing edge of the wave steepens and an internal wave reminiscent of a mode-1 elevation wave is formed at the rear of the wave, possibly due to second-order nonlinear processes which become important as the depression enters shallower water (Lamb 1994). At T5, the tidal flow switches to the

flood phase and strong mixing on the left shoal destroys the wave depression (Fig. 2i). At the late flood tide T6, the wave completely disappears (Fig. 2j).

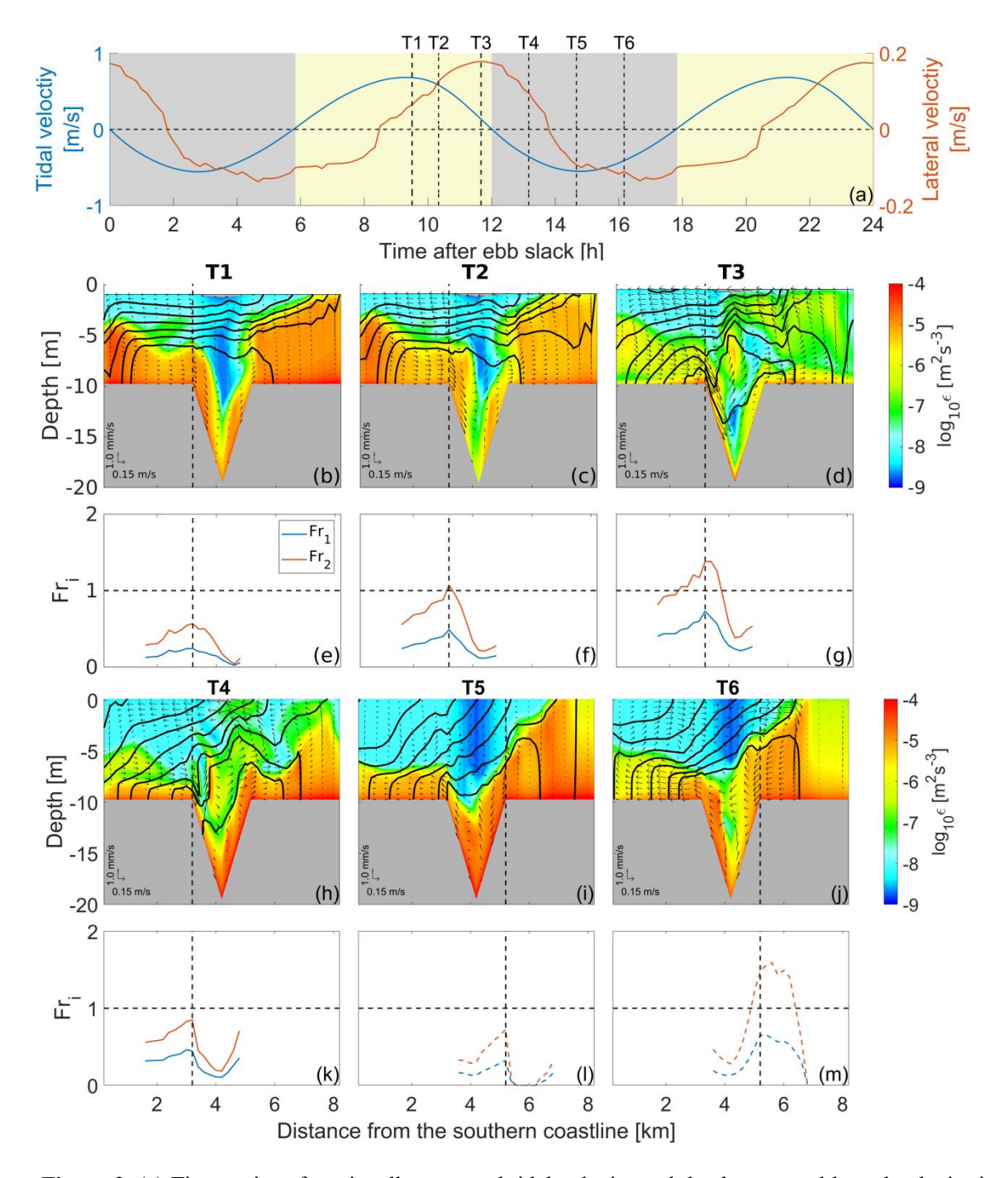


Figure 2. (a) Time series of sectionally averaged tidal velocity and depth-averaged lateral velocity in the bottom layer for run 13 with $\eta_t = 0.8$ m and $U_r = 0.03$ m/s. Vertical lines indicate the timing of the six cross-channel snapshots shown below. The grey shaded region represents flood tide and the yellow shaded region represents ebb tide. (b)-(d), (h)-(j) Distributions of salinity (contours), velocity vectors (arrows), and dissipation rate (background color) at the mid-estuary cross-section at times T1-T6 marked in (a). Contour intervals are at 1 psu increments. (e)-(g), (k)-(m) Cross-channel distribution of Froude number Fr_1 and Fr_2 at T1-T6. The solid lines indicate rightward bottom flows and the dashed lines indicate leftward bottom flows. The vertical dashed lines in (b)-(m) mark the location of the channel-shoal interface.

The time-depth distributions of the vertical velocity (w) and salinity at three locations in the mid-estuary cross-section further illustrate the propagation and evolution of the internal lee wave (Fig. 3). Site A is on the left flank of the deep channel; site B is located at the left channel-shoal interface; and site C is farther left on the left flat shoal. The magenta isohaline contours in Fig. 3a show a mode-2 wave at site A. The wave speed is ~ 0.13 m s⁻¹ relative to the background flow, while the lateral flow velocity is up to 0.17 m s⁻¹. Hence the wave is trapped at site A for about 1.5 hours due to opposing lateral currents. At T7 the trailing edge of the wave arrives at site A. From T7 to T8, the lateral velocity drops from 0.10 m s⁻¹ to 0 and then switches its direction to -0.1 m s⁻¹, such that the background flow changes from resisting the leftward wave propagation to assisting it. It takes about 1 hour for the mode-2 wave to travel from site A to site B (400 m distance), at a mean speed of 0.11 m s⁻¹ (Fig. 3b). The maximum w decreases from 1.3 mm s⁻¹ at site A to 0.8 mm s⁻¹ at site B. It takes another hour for the wave to travel to site C further left on the shoal (Fig. 3c). The wave also propagates upward during this transit (compare Figs. 3b and 3c). The maximum value of w decreases to 0.3 mm s⁻¹ at site C, which is almost one order of magnitude smaller than that at site A, signaling a significant loss of the wave energy.

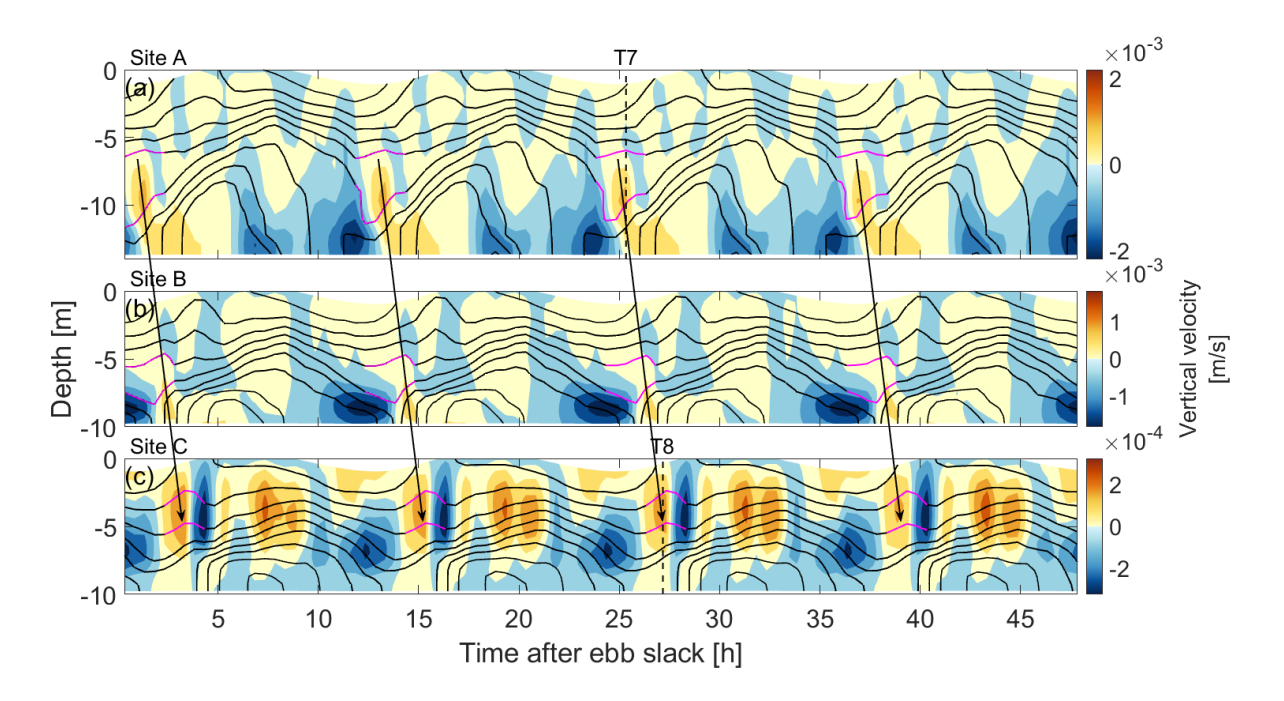


Figure 3. (a)-(c) Time-depth distributions of the salinity (contours) and vertical velocity (color) at sites A, B, and C in the mid-estuary cross-section (their locations marked in Fig. 1b). The magenta

contours highlight the internal waves.

Figures 2 and 3 show isohaline patterns reminiscent of mode-1 and mode-2 waves. To quantify the wave modal structure, a modal decomposition was performed for the vertical velocity at sites A and C. Contribution of each mode can be determined by solving a weighted least squares problem (Nash et al. 2005),

$$w(z) = \sum_{i=1}^{m} W_i \Phi_i(z), \tag{5}$$

where W_i is the *i*th modal amplitude of vertical velocity w, $\Phi_i(z)$ is the *i*th mode structure function and m is the number of modes attained from equation (4). At site A and T7, mode-2 explains 45% of the total vertical velocity variance and mode-1 explains 12% (Fig. 4a), indicating a dominant mode-2 wave consistent with the bulge structure seen in the isohaline pattern (Fig. 3a). At site C, the mode-1 structure explains 60% while mode-2 structure explains 24% (Fig. 4b), indicating a predominant mode-1 wave consistent with the elevation wave pattern seen in the isohaline (Fig. 3c). Hence the lee waves shown in Fig. 3 are strictly a mixture of mode-1 and mode-2 waves but with one mode dominating.

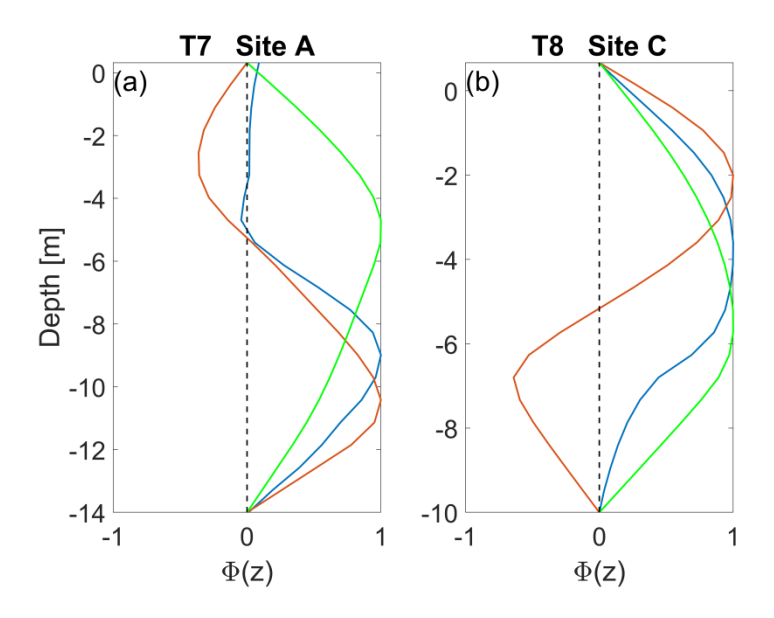


Figure 4. (a)-(c) The vertical structure of the vertical velocity normalized by its maximum value (blue), mode-1 structure function $\Phi_1(z)$ (green) and mode-2 structure function $\Phi_2(z)$ (red) at times T7 and T8 (marked in Fig. 3) and sites A and C respectively.

In contrast to the ebb tide, no internal lee waves are generated during the flood tide. The

strong bottom boundary mixing over the right shoal extends from the bottom almost to the surface (Figs. 2i & 2j). Despite the strong leftward bottom lateral flows across the right channel-shoal interface, stratification in the bottom water (below 5 m depth) over the right shoal is too weak (Fig. 2j) such that no stratified water is advected from the shoal to the deep channel. Consequently, the flood tide is not conducive to internal lee wave generation. Only one lee wave is generated over a flood-ebb tidal cycle.

It is interesting to note that the internal lee wave leads to localized high energy dissipation rate in the stratified water over the deep channel (Figs. 2d & 2h). At the slack tide T3, a pocket of relatively high ε is found under the upper crest of the mode-2 wave while the bottom boundary layers on the two shallow shoals nearly disappear (Fig. 2d). Similarly, a region of high energy dissipation with $\varepsilon \sim 3.2 \times 10^{-5}$ m² s⁻³ coincides with the steepening of isohalines at the left edge of the deep channel at T4 (Fig. 2h). Although these regions are considerably smaller the bottom boundary layers generated by tidal currents moving over the shallow shoals, the wave-induced turbulent dissipation enhances mixing in the stratified region in the estuary and could play an important role in the circulation dynamics.

3.2 Along-channel variations in wave generation

The analysis above focuses on the mid-estuary cross-section. To investigate the wave generation across different salinity regimes in the estuary, we first selected three cross-sections: a lower-estuary section ($L_1/4$), mid-estuary section ($L_1/2$) and upper-estuary section ($3/4L_1$), respectively, and followed the evolutions of the lateral velocity and salinity fields over time (Fig. 5). Internal waves appear at all the three sections, but the wave amplitude and timing of wave generation are different. At T9 when $Fr_2 = 1.2$ at the lower-estuary section (Fig. 5a), an internal lee wave with an amplitude of 2.7 m is generated over the left edge of the deep channel at the lower-estuary (Fig. 5d), while the lateral flows at the mid-estuary and upper-estuary remain subcritical (Figs. 5b & 5c). Since the salinity field in the estuary changes over a tidal cycle, it is difficult to measure the internal wave amplitude by tracking the vertical isopycnal displacements (Martin et al. 2005). Instead we calculated

the wave amplitude Δh using the maximum depth difference of the lateral velocity maxima (see Fig. 5d for an illustration of this method), following the approach by Legg and Klymak (2008). When Fr_2 at the mid-estuary section becomes supercritical at T10 (Fig. 5b), an internal lee wave of 4.6 m is generated at the mid-estuary (Fig. 5h). In the meantime, the internal lee wave generated at the lower-estuary section propagates toward the shoal (Fig. 5g) and the lateral flows at the upper-estuary section approaches critical (Fig. 5c). At T11, an internal lee wave of 8.4 m is generated by the supercritical lateral flows at the upper-estuary section (Fig. 5l), while the internal lee waves at the lower-estuary and mid-estuary sections are propagating onto the shallow shoal (Figs. 5j & 5k).

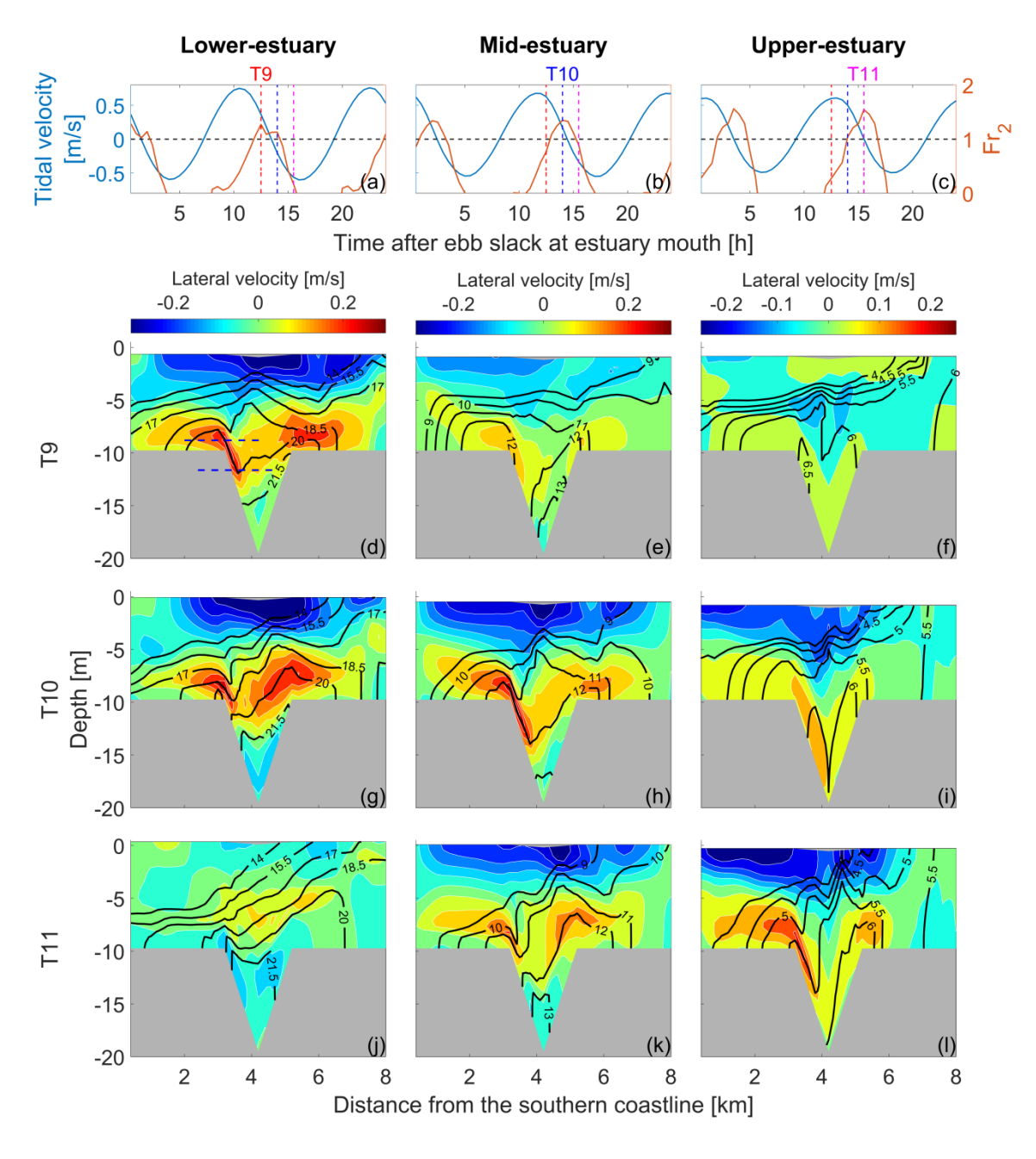


Figure 5. (a)-(c) Time series of sectionally averaged along-channel velocity (blue) and mode-2 Froude number Fr_2 (red) at the left channel-shoal interface in the upper-, mid- and lower-estuary cross-sections (their locations marked in Fig. 8). (d)-(l) Snapshots of lateral velocity (color) and salinity distribution (contours) at these sections [here timing marked as the dotted black lines in (a)-(c)]. Contour intervals are at increments of 1.5 psu in (d), (g), and (j), 1 psu in (e), (h), and (k), 0.5 psu in (f), (i), and (l). In (d) the two dashed lines mark the depths of the lateral velocity maxima and their distance is used to calculate the wave amplitude.

As shown in Fig. 5, internal lee waves can be generated at different regions of the estuary across a range of salinity regimes (5 - 20 psu). To illustrate how the lee waves vary from the mouth to the head of the estuary, we plot the along-channel distribution of the wave amplitude Δh in Fig. 6. Δh is about 3 m in the lower estuary (within ~ 45 km from the estuary's mouth), increases linearly to 6 m in the mid-estuary (45 - 90 km), and peaks around 8 m at 110 km before rolling off to 4 m in the upper estuary (Fig. 6a). This along-channel variation in the wave amplitude is consistent with an interpretation based on the maximum Froude number at the left channel-shoal interface during a tidal cycle ($Fr_{2\text{max}}$). V decreases from the lower-estuary to the upper-estuary, which goes in an opposite direction to Δh (Fig. 6b). However, the depth-averaged stratification (N^2) at the left channel-shoal interface decreases faster in the along-channel direction, indicating that the wave amplitude depends on the competition between the lateral velocity and stratification. $Fr_{2\text{max}}$ increases gradually from the lower-estuary to the upper-estuary before rolling off (Fig. 6c). Moreover, $Fr_{2\text{max}}$ exceeds 1 in most parts of the estuary, affirming that supercritical lateral flows are a pre-condition for the internal lee wave generation. In the most upstream region of the estuary (130-150 km), stratification is too weak to support the internal wave generation. In addition, the time when the lateral flows become critical $(T_{Fr_2=1})$, corresponding to the timing of the lee wave generation at different parts of the estuary (Fig. 6d), can be fit as

$$T_{Fr_2=1} \approx \frac{x}{\sqrt{gD}} + 10, \tag{7}$$

where x is the distance from the estuary mouth, g is the gravity acceleration and D is the water depth at the shoals, as the tidal wave propagates upstream and produces lateral flows that interact with stratified water over topography to generate the internal lee wave.

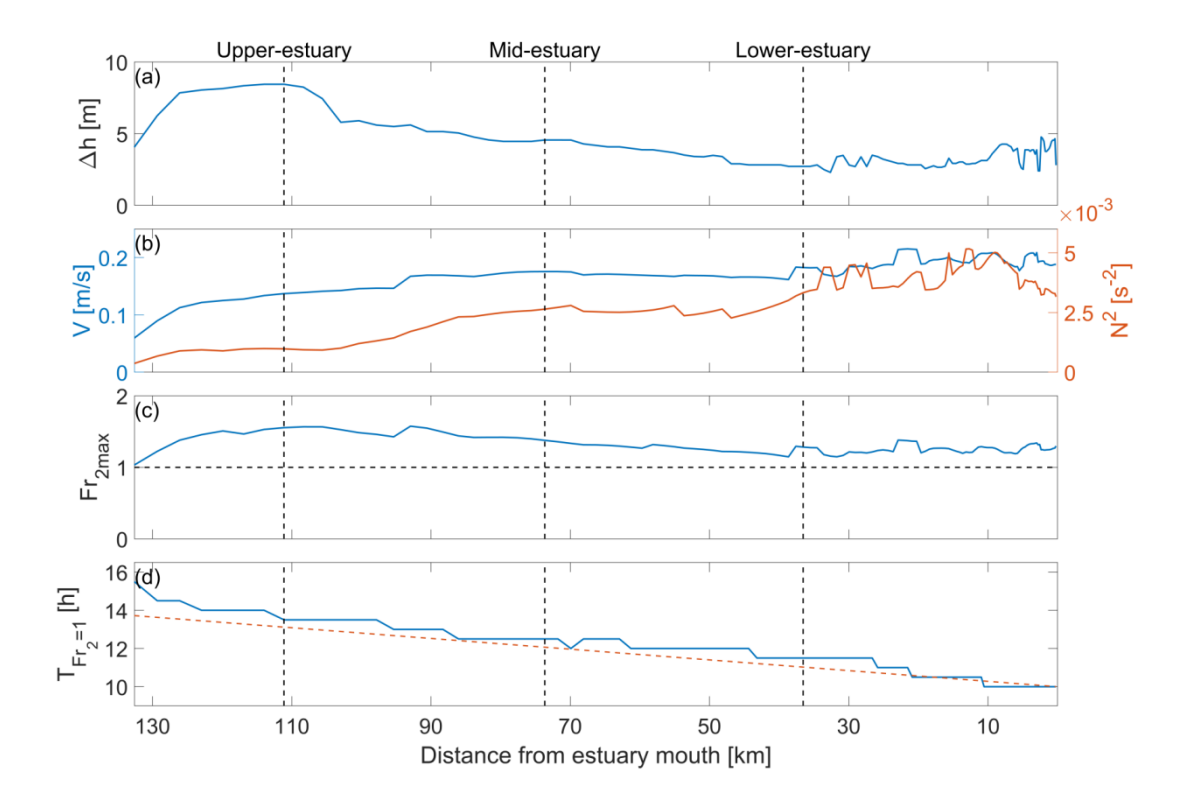


Figure 6. Along channel distributions of (a) internal lee wave amplitude Δh , (b) maximum bottom lateral velocity V and the depth-averaged stratification N^2 when Fr_2 reaching maximum at the left channel-shoal interface, (c) maximum mode-2 Froude number $Fr_{2\text{max}}$, and (d) the timing of lateral flow reaching critical condition ($T_{Fr_2} = 1$) after ebb slack at estuary mouth. The red dashed line in (d) indicates the function of $\frac{x}{\sqrt{gD}}$ +10. The black dashed lines mark the locations of upper-, mid- and lower-estuary cross-sections respectively.

4. Internal lee wave generation under different hydrodynamic conditions

Since the internal lee wave generation depends on the stratification and lateral current speed, we ran the model over a range of tidal amplitudes and river flows and identify the hydrodynamic conditions that might be conducive to the lee wave generation.

4.1 Effects of river flow

Figure 7 shows the results from 4 model runs with a fixed offshore tidal amplitude $\eta_t = 0.6$ m but at different values of the river flow: $U_r = 0.01$, 0.03, 0.05 and 0.07 m s⁻¹ (runs 7 - 10 in Table 1). These snapshots are taken at the time when Fr at the left channel-shoal interface reaches the maximum during the ebb tide and the isohaline displacement is nearly

largest. At $U_r = 0.01$ m s⁻¹, $Fr_{2\text{max}} = 1.15$ and Δh is 4.4 m while the depth-averaged stratification (N^2) is 3.2×10^{-3} s⁻² (Fig. 7a). At $U_r = 0.03$ m s⁻¹, N^2 increases to 5.3×10^{-3} s⁻², $Fr_{2\text{max}} = 1.0$ and Δh decreases to 1.3 m (Fig. 7b). At higher river flows ($U_r = 0.05$, 0.07 m s⁻¹), the estuary becomes highly stratified ($N^2 = 5.9 \times 10^{-3}$, 6.3×10^{-3} s⁻²) and the lateral flow remains subcritical such that no significant perturbations of isohalines are seen over the left channel-shoal interface (Figs. 7c-d). At a fixed tidal amplitude, both $Fr_{2\text{max}}$ and Δh decrease as the river discharge increases.

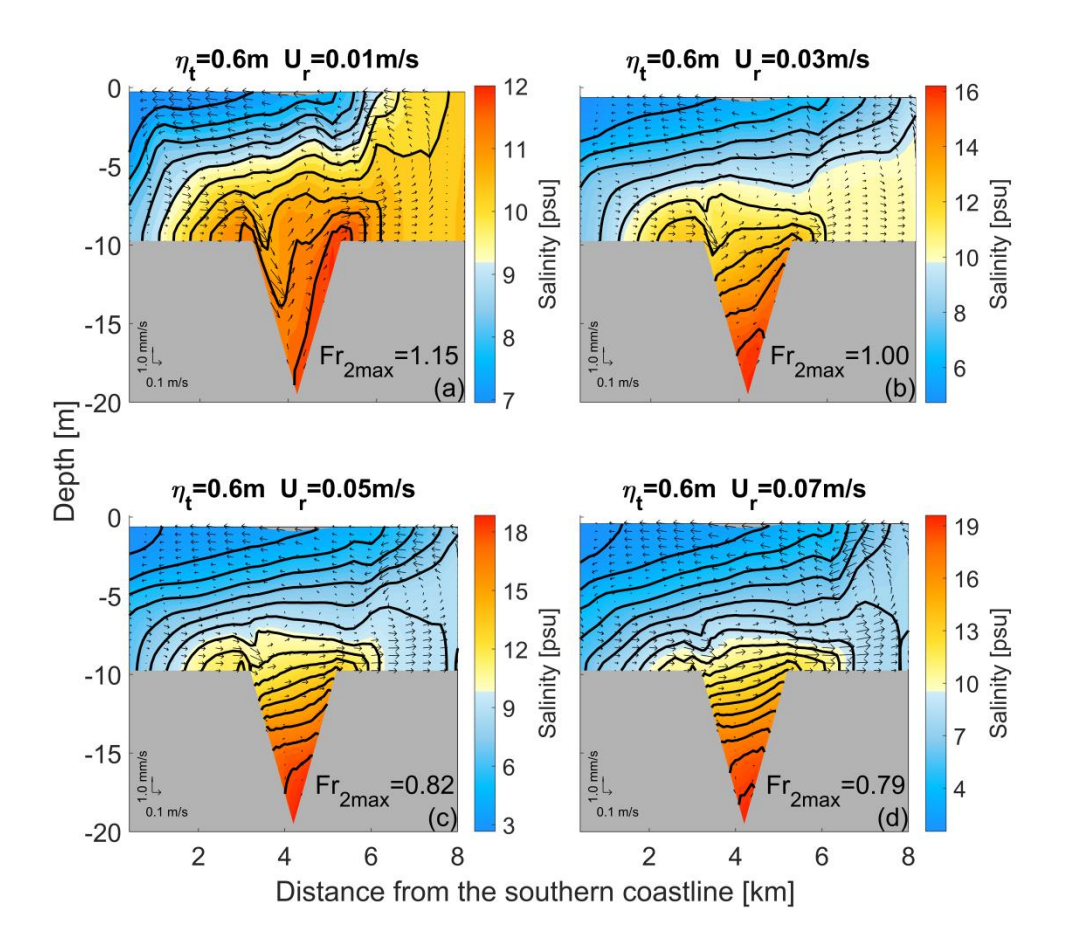


Figure 7. (a)-(d) Snapshots of cross-channel distributions of salinity (contours) and lateral velocity (arrows) at the mid-estuary section in model runs with different river discharges but fixed tidal forcing (runs 7–10). Contour interval is 0.5 psu in (a), and 1 psu in (b)-(d). The snapshots are taken at the time when Fr_2 at the left channel-shoal interface reaches a maximum.

The river flow affects the generation of internal lee wave mainly through its effects on stratification (Fig. 8). At a fixed tidal amplitude, the stratification increases with U_r : N^2 at the channel-shoal interface in the mid-estuary section increases from $(2.5 - 3) \times 10^{-3}$ s⁻² at $U_r = 0.5 \times 10^$

 0.005 m s^{-1} to $(5.5 - 7) \times 10^{-3} \text{ s}^{-2}$ at $U_r = 0.07 \text{ m s}^{-1}$ (Fig. 8a). The internal wave phase speed c_i depends on the stratification and also increases with U_r (Fig. 8b). The mode 2 wave phase speed, c_2 , increases from 0.08 m s^{-1} at low river discharge to $0.12 - 0.14 \text{ m s}^{-1}$ at high river discharge. Therefore, it is harder for the lateral flow to reach a critical speed and the internal lee wave to develop as the river discharge increases.

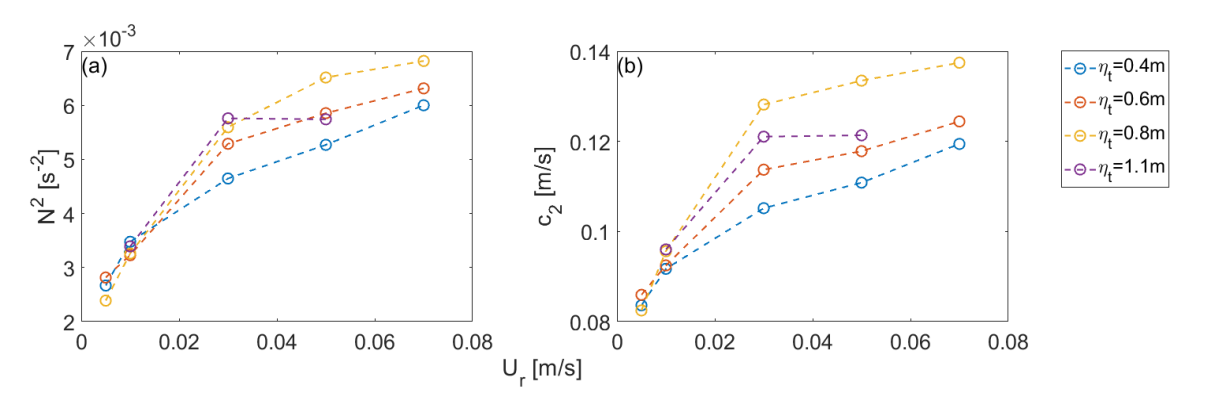


Figure 8. (a) The stratification at the left channel-shoal interface and (b) the internal lee wave phase speed as a function of river discharge U_r . Values are calculated at the mid-estuary section from the model runs featuring internal waves (runs 1-15, 17-19).

4.2 Effects of tidal amplitude

The internal lee wave shows a nonlinear response to increasing tidal amplitude η_t at a fixed river flow ($U_r = 0.01 \text{ m s}^{-1}$) (Fig. 9). $Fr_{2\text{max}}$ does not increase monotonically as η_t increases. As η_t increases from 0.6 to 0.8 m, $Fr_{2\text{max}}$ increases from 1.15 to 1.5 and the internal wave amplitude Δh increases from 4.4 to 5.7 m (Figs. 9a & 9b). The maximum lateral flow velocity increases from 0.106 to 0.143 m s⁻¹ while the stratification is relatively unchanged. However, when η_t is 1.1 m, the maximum lateral flow velocity decreases slightly to 0.140 m s⁻¹, $Fr_{2\text{max}}$ decreases slightly to 1.46, and wave amplitude Δh decreases to 4.9 m (Fig. 9c). In these three model runs stratification persists on the shallow left shoal and deep channel, creating a condition favorable for the lee generation when the lateral currents advect the stratified water from the left shoal to the deep channel. One also notices pockets of high vertical diffusivity K_v in Figs. 9b and 9c where the lee wave steepens to produce localized strong mixing, in addition to high K_v in the bottom boundary layer on the shoals. When η_t reaches 1.3 m, however, water on both left shallow shoals becomes well-mixed and stratification is confined to the deep channel (Fig. 9d). The maximum lateral flow velocity

decreases to 0.094 m s⁻¹. No internal waves are generated but salinity fronts are developed over the channel-shoal interfaces.

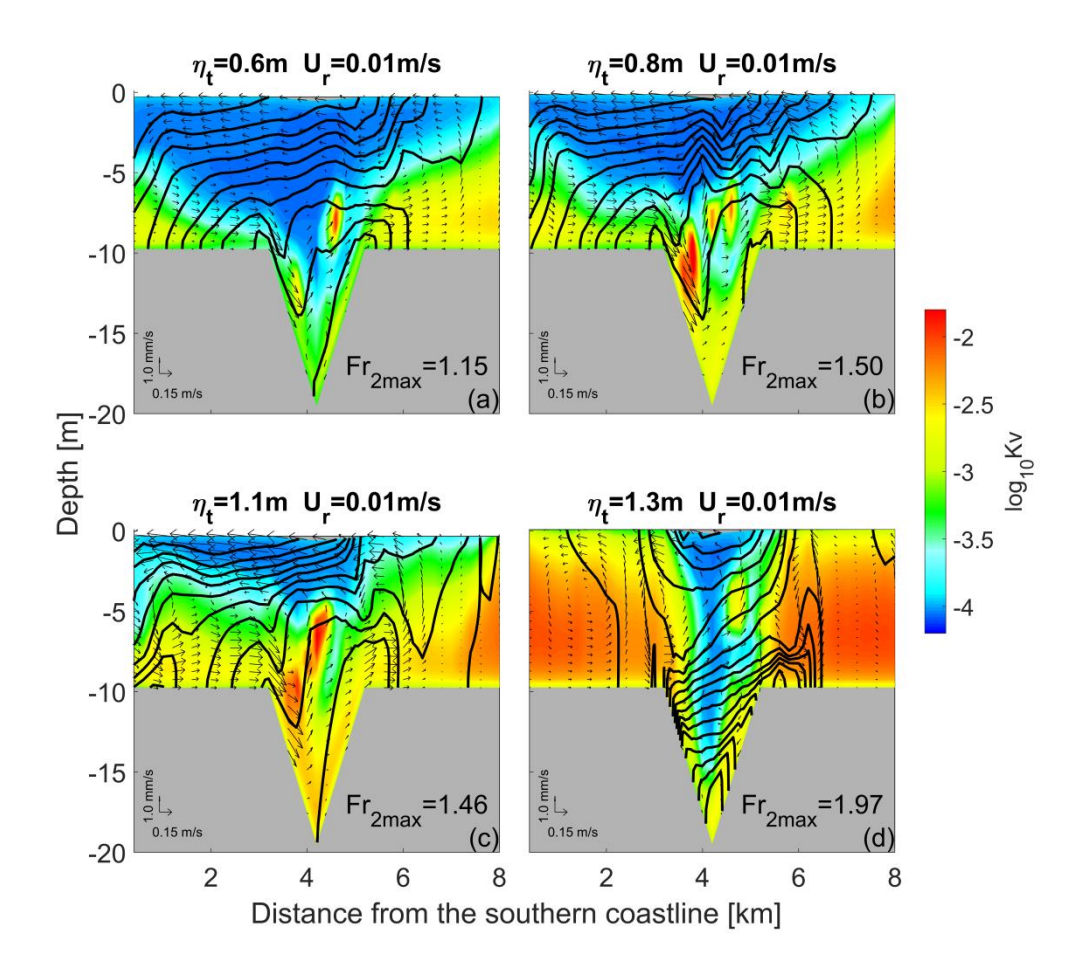


Figure 9. (a)-(d) Snapshots of cross-channel distributions of time-averaged viscosity K_{ν} during the ebb tide (background color), salinity (contours), and lateral velocity (arrows) at the mid-estuary section in model runs with different tidal amplitudes but fixed river discharge (runs 7, 12, 17, 22). Contour interval is 0.5 psu.

This nonlinear relationship between the internal wave amplitude and tidal amplitude η_t can be attributed to the nonlinear response of the lateral circulation to changes in the magnitude of tidal currents. As η_t increases, the maximum lateral flow velocity V increases first but then saturates or even decreases slightly (Fig. 10). The lateral circulation strength depends on the balance among three terms: the generation of streamwise vorticity by lateral Ekman forcing, the lateral baroclinic forcing and the vertical diffusion (Li et al. 2014). Although a stronger tidal flow produces stronger vorticity generation, it also leads to stronger vorticity diffusion that tends to spin down the lateral circulation (see the region of high K_V

expanding from Fig. 9a to Fig. 9d). As a result, the lateral velocity initially increases as η_t increases from 0.6 to 0.8 m but then decreases as η_t increases to 1.1 and 1.3 m. Since the lee wave is generated by the lateral currents, Δh also shows a parabolic response to the tidal amplitude.

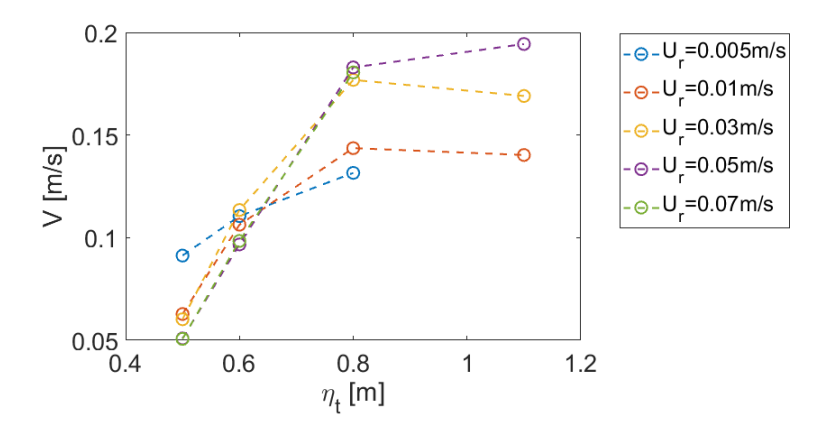


Figure 10. The maximum bottom lateral velocity as a function of tidal velocity at the estuary mouth η_t . Values are calculated at the mid-estuary section from the model runs featuring internal waves (runs 1-15, 17-19).

At $U_r = 0.01$ m s⁻¹, strong turbulent mixing destroys stratification over the shallow shoals when the tidal amplitude η_t reaches 1.3 m, thereby inhibiting the generation of the internal lee wave (Fig. 9d). This remains true at all the river flows: no internal waves could be generated when tidal currents are strong enough to erase stratification on the shoals. Due to the effects of the Coriolis force, brackish water typically hugs along the southern (left) boundary as it moves seaward, setting up stratification over the left shoal. During the ebb tide, the lateral currents advect this stratified water to the deep channel and generate the internal lee wave. When the tidal currents are very strong, however, K_v reaches O(10⁻²) m² s⁻¹ on the shallow shoals such that turbulence completely mixes the water column there (Fig. 9d). The vertical stratification is confined to the deep channel and salinity fronts separate the stratified water over the deep channel from the well-mixed water on the two shoals.

4.3 Different wave structures

In addition to changes in the wave amplitude, wave structure also changes under different

river flow and tidal conditions. The isohalines in Fig. 9c plunge into the deep channel and then rebound abruptly as an internal hydraulic jump, with the eddy diffusivity reaching O(10⁻²) m² s⁻¹. A time sequence of snapshots in Fig. 11 illustrates the generation process of this hydraulic jump. The downslope flow causes the isohaline marked as the white contour line to depress (Fig. 11b) when the bottom lateral flows just become supercritical (Fig. 11e). As the lateral flow strengthens, the depression wave grows in amplitude over the left edge of the deep channel (Fig. 11c). On the other hand, the lateral flows in the deeper center channel are subcritical (Fig. 11f). The transition from the supercritical to subcritical flows is accomplished via a hydraulic jump with the isohalines at the trailing edge lifted sharply upward (Fig. 11c). As the lateral flows at the channel-shoal interface get weaker and become subcritical during the flood tide (Fig. 11g), the hydraulic jump propagates onto the left shoal (Fig. 11d). This sequence of events is similar to the internal hydraulic jump generated by tidal flow over a tall steep ridge in the deep ocean (Legg and Klymak 2008, Klymak et al. 2008), with the accompanied strong local mixing.

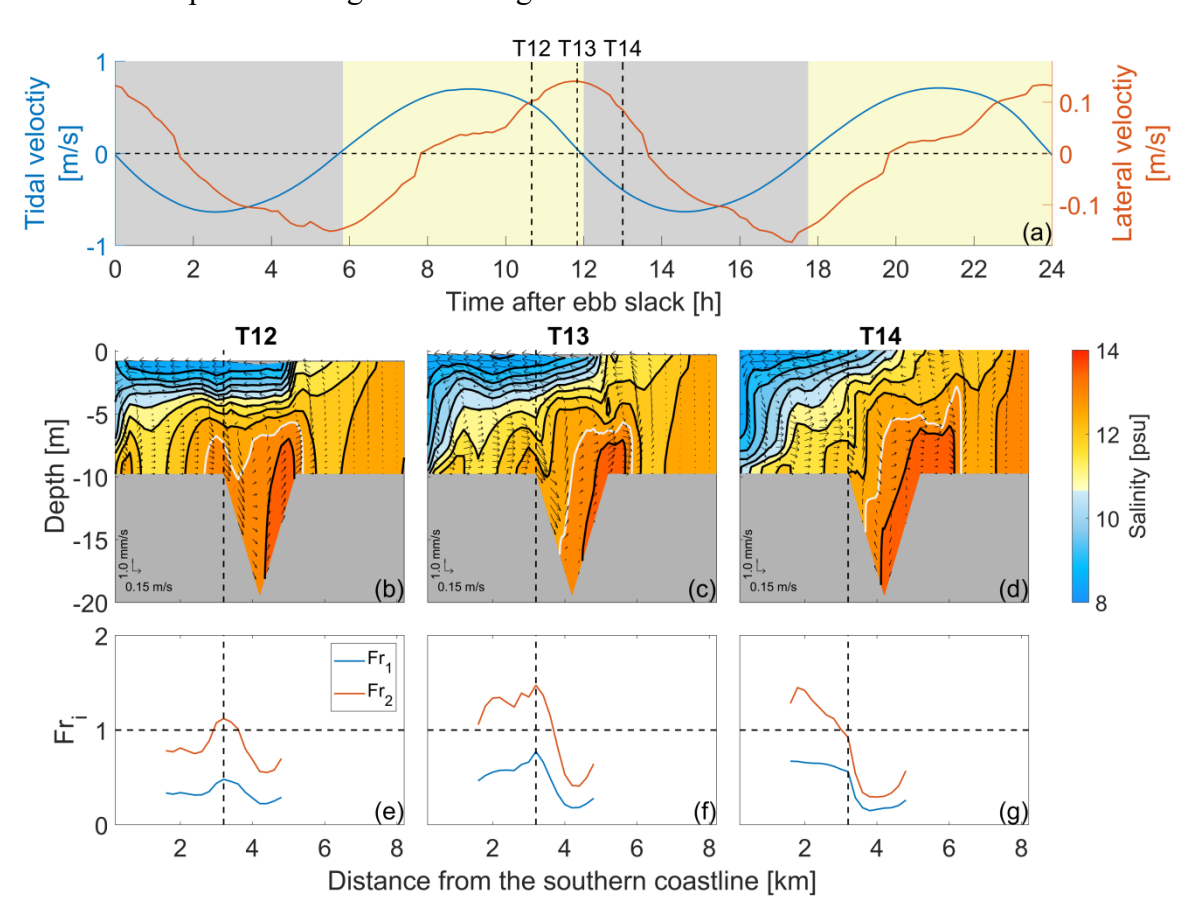


Figure 11. (a) Time series of sectionally averaged tidal velocity and depth-averaged lateral velocity in the bottom layer for run 17 with $\eta_t = 1.1$ m and $U_r = 0.01$ m/s. (b)-(d) Distributions of salinity (contours) and

velocity vectors (arrows) at the mid-estuary cross-section at times T12-T14 marked in (a). Contour intervals are at 0.5 psu increments. White contour lines mark the isohaline of 13 psu. (e)-(g) Cross-channel distribution of Froude number Fr_1 and Fr_2 at T12-T14.

In addition to mode-2 lee wave and hydraulic jump, a wave in the form of a mode-1 depression can be generated when both tidal amplitude and river discharge are large. An example is found in run 15 with $U_r = 0.07$ m s⁻¹ and $\eta_t = 0.8$ m. At T15 a small-amplitude mode-2 wave is generated well above the left edge of the deep channel as Fr_2 reaches 1 (Fig. 12b). No wave perturbations can be seen in the isohalines in the deep channel due to the establishment of strong stratification there. As the lateral flows strengthen and Fr_1 approaches 1, a mode-1 depression wave appears near the left edge of the deep channel (Fig. 12c). This mode-1 wave subsequently propagates onto the shallow shoal as the lateral currents weaken (Fig. 12d). It is interesting to note that the heavier stratified flow in the deep channel becomes stagnant, with the lateral velocity dropping to near zero. The rightward lateral currents on the left shoal run across the top of the deep channel, causing the isohalines near the right edge of the deep channel to tilt up (Figs. 12b-d). In the meantime, the downward tilt of the isohalines on the left edge of the deep channel leads to the generation of a mode-1 depression wave in the stratified water above (Figs. 12c). The heavy stratified water in the deep channel is essentially decoupled from the flows above. This flow pattern is very different from stratified flows over a sill in the ocean but is similar to stratified flows over a valley in the atmosphere (Baines 1995, Lehner et al, 2016a, b, Rotunno and Lehner 2016).

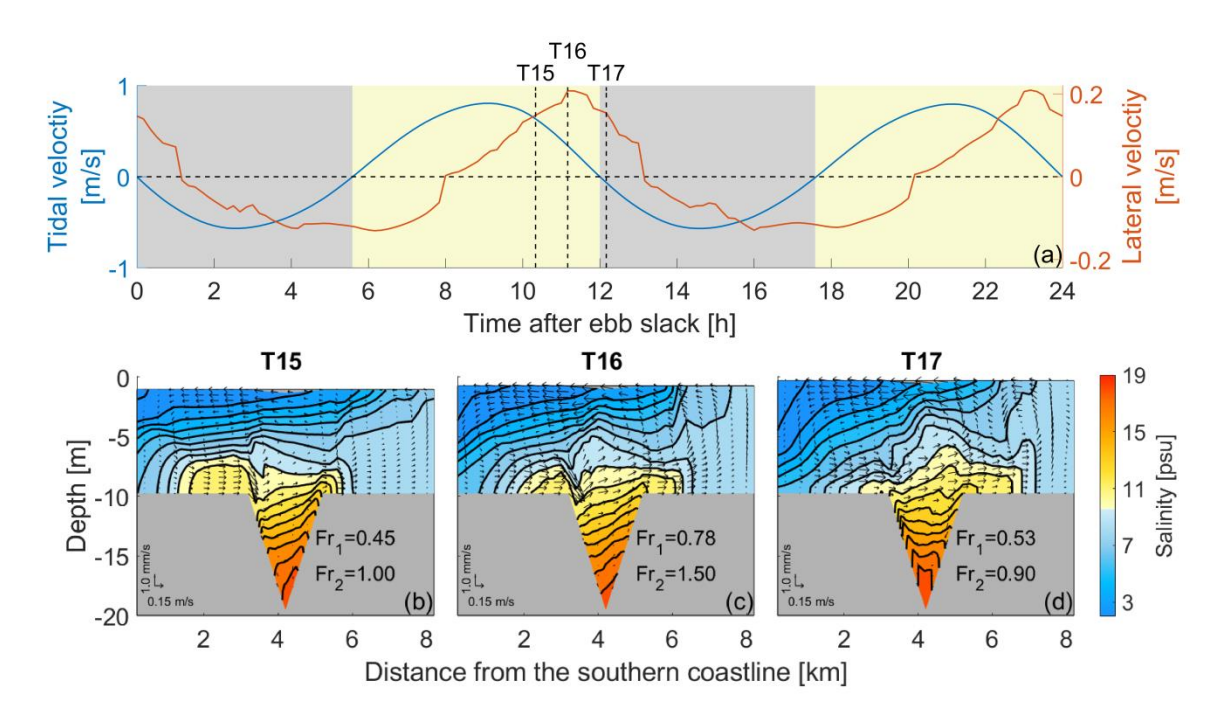


Figure 12. (a) Time series of sectionally averaged tidal velocity and depth-averaged lateral velocity in the bottom layer for run 15 with $\eta_t = 0.8$ m and $U_r = 0.07$ m/s. (b)-(g) Distributions of salinity (contours) and velocity vectors (arrows) at the mid-estuary cross-section at times T15-T17 marked in (a). Contour intervals are at 1 psu increments.

4.4 Interpretation in terms of internal hydraulics

We calculated the wave amplitude Δh at 10 cross-sections of the estuary from all the model runs featuring the internal lee waves (runs 1-15, 17-19) and plot it against $Fr_{2\text{max}}$. Figure 13a shows that Δh ranges between 1 and 8 m when $Fr_{2\text{max}} > 1$. Waves of smaller amplitude are also found when $0.5 < Fr_{2\text{max}} < 1$. In the laboratory experiments Maxworthy (1979) also observed internal lee waves at those smaller values of the Froude number. For a tidal flow over a sill, Fr can be calculated using the vertically averaged tidal velocity and the wave phase speed estimated from the background stratification (Farmer and Smith 1980). Here the calculation of Fr is more complicated due to the two-layer lateral flows and varying stratification (see Eq. 6). Nevertheless, the generation of internal lee waves as shown in Figs. 2, 5, 6, 7 and 9 is highly consistent with an interpretation base on the internal hydraulics, although the Fr threshold is not necessarily identical to 1 due to the uncertainty in estimating $Fr_{2\text{max}}$ and the previous observation indicating that small amplitude lee waves can still be generated when Fr falls below 1. Nevertheless, the wave amplitude does not show a simple relationship with $Fr_{2\text{max}}$: e.g., Δh varies from 1 to 8.5 m at $Fr_{2\text{max}} = 1.5$.

On the other hand, V/\overline{N} provides a reasonable scaling for the wave amplitude, where V is the maximum lateral flow velocity and \overline{N} is the sectionally averaged buoyancy frequency over the deep channel at the time of $Fr_{2\text{max}}$. It sets a limit on the maximum possible isopycnal displacement since the conversion of the potential energy of a displaced isopycnal in the lee wave to the kinetic energy takes place within V/\overline{N} , based on the energetics argument (Mayer and Fringer 2017). In Fig. 13b Δh varies approximately linearly with V/\overline{N} when $V/\overline{N} > 1.7$. We calculated the lee wave Froude number $\overline{N}H/V$ for all the model runs (Legg 2021) where H is the height of the deep channel (see Fig. 1b). Table 1 shows that $\overline{N}H/V$ varies between \sim 2 and \sim 18, indicating that the generated lee waves are highly nonlinear. In this regime, Legg and Klymak (2008) also found that Δh scales with V/\overline{N} in their simulations of tidal flows over a tall ridge in the deep ocean.

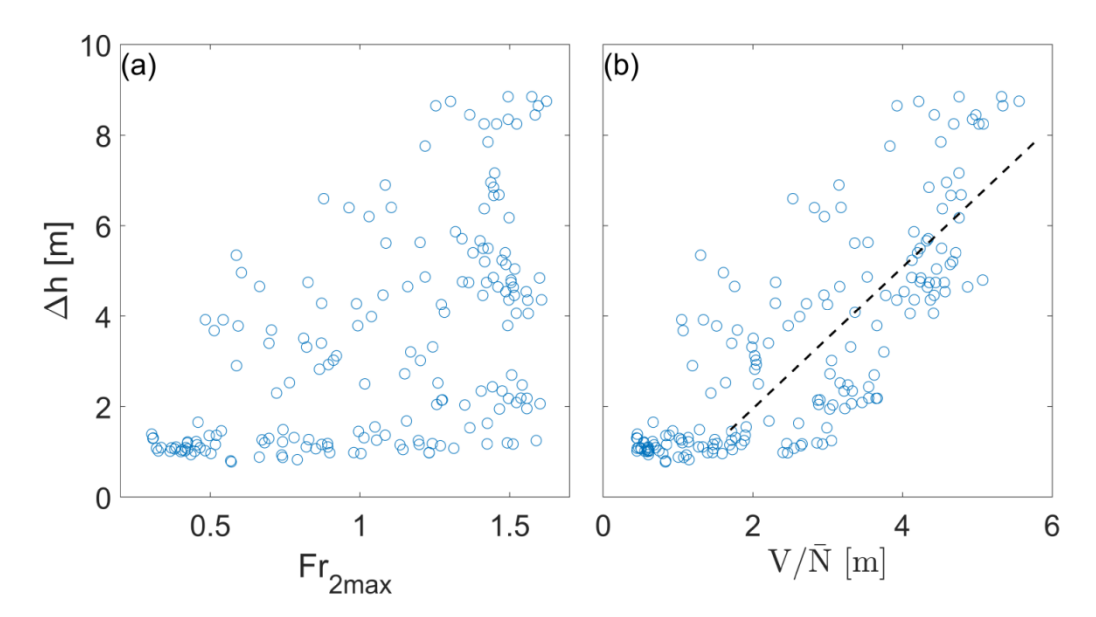


Figure 13. Internal lee wave amplitude Δh versus $Fr_{2\text{max}}$ (a) and V/\overline{N} (b) from all model runs featuring internal waves. The black dashed line in (b) is a linear fit for $V/\overline{N} > 1.7$. In the model runs, 10 cross-sections are selected to spread over the entire estuary, at a distance of (1 to 10)/(10 L_1) from the mouth of the estuary. Each open circle represents Δh calculated from a cross-section, along with $Fr_{2\text{max}}$, V and \overline{N} .

5. A regime diagram

To put in a broader context, the model results are organized in terms of the freshwater Froude number Fr_f and the estuarine mixing parameter M that are used to classify different types of estuaries (Geyer and MacCready 2014). The freshwater Froude number Fr_f is defined as

$$Fr_f = \frac{U_r}{\sqrt{g\beta S_{ocean}h}},\tag{5}$$

where U_r is the river flow velocity, β is the saline contraction coefficient, S_{ocean} is the oceanic salinity, and h is the mean water depth. Fr_f measures the strength of the river flow against the maximum possible frontal propagation speed in an estuary. The mixing parameter M is defined as

$$M^2 = \frac{C_d U_t^2}{\omega N_0 h^2},\tag{6}$$

where C_d is bottom drag coefficient, U_t is the amplitude of depth-averaged tidal current velocity, and $N_0 = (g\beta S_{ocean}/h)^{1/2}$ is the buoyancy frequency for maximum top-to-bottom salinity variation in an estuary. M quantifies the effectiveness of tidal mixing.

Mapping the internal wave amplitude in the $Fr_f - M$ parameter space helps identify which types of estuaries might be conducive to internal lee wave generation (Fig. 14). At a fixed value of M, the normalized wave amplitude $\Delta h/H$ decreases with increasing Fr_f as stronger river flow leads to stronger stratification that tends to suppress waves. No internal waves are generated when $Fr_f > 0.03$. At a fixed value of Fr_f , $\Delta h/H$ initially increases with increasing M but decreases or saturates to a certain amplitude as M further increases. This results from the nonlinear dependence of the lateral circulation strength on the tidal amplitude. Geyer and MacCready (2014) classified different types of estuaries in the $Fr_f - M$ parameter space. In the regime of strongly stratified estuaries on the left (shaded in dark green color), $\Delta h/H$ decreases from 0.7 to 0 as Fr_f increases from 0.003 to 0.03. When $Fr_f > 0.03$, river flows produce strong stratification such that the lateral flows remain to be subcritical throughout the tidal cycle and no lee waves can be generated (Fig. 14a). On the other hand, $\Delta h/H$ increases with increasing M because stronger tides lead to stronger lateral flows in this regime. In partially mixed estuaries in the middle (shaded in light green color), internal lee waves can be generated over a larger part of the parameter space. Most of the lee waves generated in the

strongly stratified and partially mixed estuaries are mode-2 waves (Fig. 14d). With increasing Fr_f , $\Delta h/H$ still decreases, as the strong stratification in the deep channel suppresses the wave growth. Under medium M and large Fr_f , wave structure also changes into mode-1 wave due to the strongly stratified water in the deep-channel that becomes stagnant and uncoupled with the flows above (Fig. 14b). At lower values of Fr_f , $\Delta h/H$ first increases with M, reaches a maximum around $M \approx 0.6$ and then decreases when M increases further. The wave structure changes into hydraulic jump when M > 0.6 as the flow transitions from a supercritical flow on the shoal to a subcritical flow in the deep channel (Fig. 14e). However, $\Delta h/H$ becomes nearly independent of M when $Fr_f > \sim 0.02$. No internal waves are found under the regime for periodically stratified estuaries. Water on the shoals becomes well mixed and salinity fronts are developed to separate the well-mixed shallow shoals from the stratified deep channel (Fig. 14f).

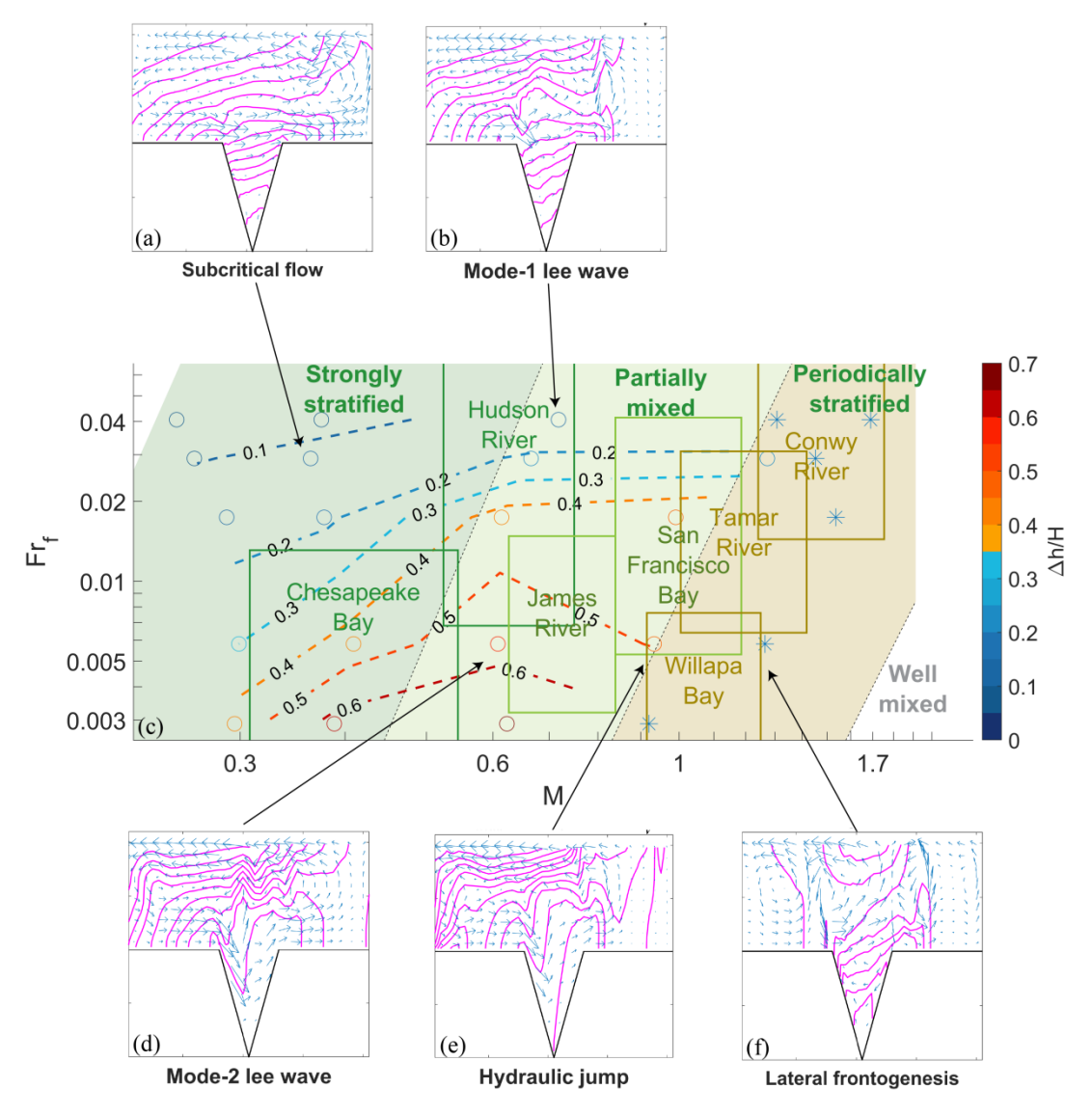


Figure 14. Regime diagram of normalized wave amplitude $\Delta h/H$ as a function of Fr_f and M. Stars are the runs whose results show lateral frontogenesis. The black dashed lines denote the boundaries among four different estuary classes. The rectangle indicates the approximate influence of spring-neap tidal variation, river flow variation for the estuaries indicated.

6. Discussion and Conclusion

Using a numerical model for an idealized straight estuary with channel-shoal bathymetry, we investigated the generation of internal lee waves. Our study confirms that tidally-driven lateral flows can generate internal lee waves across all the salinity regimes in coastal plain estuaries featuring channel-shoal bathymetry. The wave amplitude decreases with increasing river flow as stronger stratification suppresses the lee waves. The wave amplitude however

shows a nonlinear dependence on the tidal amplitude: it initially increases with the tidal amplitude but saturates or decreases as the tide amplitude further increases. When the tidal currents become strong enough to erase stratification on the shallow shoals, no internal lee waves could be generated but fronts are developed at the channel-shoal interface.

With the lee wave Froude number $\overline{N}H/V > 1$ and the intrinsic frequency Vk between f and \overline{N} (Table 1), the lee waves generated in coastal plain estuaries fall into Regime 3 in the regime diagram of lee waves (Legg 2021). It is featured by the generation of nonlinear lee waves of vertical length scale V/\overline{N} , which agrees with the scaling shown in Fig. 13b. For stratified flows over a sill, this flow regime is also characterized by blocking, hydraulic control of the jet above the topographic crest, and the possibility of a stagnant wedge downstream of the crest, with mixing occurring primarily in the hydraulic jump downstream if present (Klymak et al. 2010, Winters 2016). Obviously no upstream blocking occurs for the stratified flow over a valley (deep channel) but the lateral flows are hydraulically controlled at the edge of the deep channel. If the flows in the deep channel are subcritical, a hydraulic jump forms with the isohalines at the trailing edge of the lee wave lifted sharply upward, producing high dissipation rate and strong mixing there (e.g. Figs. 2h and 9c). Similar to the tidal flows over a tall steep topography in the deep ocean (Legg and Klymak 2008), these hydraulic jumps may be an important mechanism for generating strong local mixing in the stratified estuary.

Most studies of lee waves in the ocean focused on stratified flows over a sill. The stratified flows over a valley (the deep channel) have received much less attention. While they share some characteristics as the flows over a sill such as the hydraulic control, they also differ in important aspects. For example, the heavier stratified water in the deep channel may become stagnant and uncoupled from the lateral flows above (Fig. 12). This flow deceleration and stagnation have been found in stratified flows over the valley when $\overline{N}H/V$ is large (Baines 1995), such as katabatic flows over a valley in the atmosphere. For example, the stratified flows over the Arizona's Meteor Crater often lead to the formation of waves and hydraulic jumps in the lee of the upwind rim (Holden et al. 2000, Leher et al. 2016a).

Numerical simulations of different valley depths and shapes revealed a rich variety of wave and flow structures, ranging from complete flows through the valley to valley-flow stagnation to situations involving internal wave breaking, lee waves, and quasi-stationary waves in the valley (Leher et al. 2016b, Rotunno and Leher 2016). Further research is needed to explore tidal flows over a valley in the ocean. The deep channel is modelled as a triangle in this paper and different geometric shapes could be considered in a future study.

To place the model results in a broad context, we plot the lee wave amplitude in the Fr_f -M parameter space. Strongly stratified and partially mixed estuaries cover a wide range of estuaries such as Hudson River and San Francisco Bay and may be conducive to the lee wave generations. According to the estuarine classification diagram by Geyer and MacCready (2014), Chesapeake Bay is a strongly stratified estuary. Indeed mode-2 internal lee waves were observed in the middle part of the estuary (Xie et al. 2017b) and the numerical simulation reproduced the mode-2 lee wave (Xie and Li 2019). Xie et al. (2017b) also observed that the lee wave subsequently propagated onto the shallow shoal and evolved into a group of internal solitary waves of elevation. A non-hydrostatic model would be required to simulate the transformation of the lee wave into solitary waves, another topic for the future research.

Acknowledgements.

We thank two reviewers for their helpful comments. We are grateful to NSF (OCE-1756155) for the financial support. This is UMCES contribution number xxxx.

Data Availability Statement.

All model results analyzed in this study have been uploaded and openly available at https://zenodo.org/record/5652345#.YYqN37pOk2w.

REFERENCES

- Baines, P.G., 1995: Topographic Effects in Stratified Flows. Cambridge Univ. Press. 482 pp.
- Bourgault, D., M. D. Blokhina, R. Mirshak, and D. E. Kelley, 2007: Evolution of a shoaling internal solitary wavetrain. *Geophys. Res. Lett.*, **34**, L03601, doi:10.1029/2006GL028462.
- Bourgault, D., and D. E. Kelley, 2003: Wave-induced boundary mixing in a partially mixed estuary. *J. Mar. Res.*, **61(5)**, 553-576.
- Cheng, P., A. Valle-Levinson, and H. E. de Swart, 2010: Residual currents induced by asymmetric tidal mixing in weakly stratified narrow estuaries. *J. Phys. Oceanogr.*, **40(9)**, 2135-2147.
- Cheng, P., A. Valle-Levinson, and H. E. de Swart, 2011: A numerical study of residual estuarine circulation induced by asymmetric tidal mixing in tidally dominated estuaries. *J. Geophys. Res.*, **116**, C01017, doi:10.1029/2010JC006137.
- Cummins, P. F., S. Vagle, L. Armi, and D. M. Farmer, 2003: Stratified flow over topography: Upstream influence and generation of nonlinear internal waves. *Proc. Roy. Soc. London.*, 459A, 1467–1487.
- da Silva, J. C. B., M. C. Buijsman, and J. M. Magalhaes, 2015: Internal waves on the upstream side of a large sill of the Mascarene Ridge: A comprehensive view of their generation mechanisms and evolution. *Deep-Sea Res. I*, **99**, 87–104, doi:10.1016/j.dsr.2015.01.002.
- Dyer, K.R., 1982: Mixing caused by lateral internal seiching within a partially mixed estuary. *Estuarine Coastal Mar. Sci.*, **15(4)**, 443-457.
- Farmer, D. M., and L. Armi, 1999: The generation and trapping of solitary waves over topography. *Science*, 283, 188–190.
- Farmer, D. M., and J. D. Smith, 1980: Tidal interaction of stratified flow with a sill in Knight Inlet. *Deep-Sea Res.*, **27A**, 239–246.

- Geyer, W. R., and P. MacCready, 2014: The estuarine circulation. *Annu. Rev. Fluid Mech.*, **46**, 175–197, doi:10.1146/annurev-fluid-010313-141302.
- Gill, A. E., 1982: Atmosphere–Ocean Dynamics. Academic Press, 662 pp.
- Gregg, M., and L. Pratt, 2010: Flow and hydraulics near the sill of Hood Canal, a strongly sheared, continuously stratified fjord. *J. Phys. Oceanogr.*, **40**, 1087–1105, doi:10.1175/2010JPO43121.
- Groeskamp, S., J. Nauw, and L. Maas, 2011: Observations of estuarine circulation and solitary internal waves in a highly energetic tidal channel. *Ocean Dyn.*, **61**, 1767–1782, doi.org/10.1007/s10236-011-0455-y.
- Hetland, R. D., and W. R. Geyer, 2004: An idealized study of the structure of long, partially mixed estuaries. *J. Phys. Oceanogr.*, **34**, 2677–2691, doi:10.1175/JPO2646.1.
- Holden, J. J., S. H. Derbyshire, and S. E. Belcher, 2000: Tethered balloon observations of the nocturnal stable boundary layer in a valley. *Bound.-Layer Meteor.*, **97**, 1–24, doi:10.1023/A:1002628924673.
- Kantha, L.H., and C.A. Clayson, 1994: An improved mixed layer model for geophysical applications. *J. Geophys. Res.*, **99**, 25235–25266.
- Klymak, J.M., R. Pinkel, and L. Rainville, 2008: Direct breaking of the internal tide near topography: Kaena Ridge, Hawaii. *J. Phys. Oceanogr.*, **38(2)**, 380-399.
- Klymak, J.M., S.M. Legg, and R. Pinkel, 2010: High-mode stationary waves in stratified flow over large obstacles. *J. Fluid Mech.*, **644**, 321-336.
- Lamb, K. 1994. Numerical experiments of internal wave generation by strong tidal flow across a finite-amplitude bank edge. *J. Geophys. Res.*, **99**, 843–864.
- Legg, S., 2021: Mixing by oceanic lee waves. Annu. Rev. Fluid Mech., 53, 173-201.
- Legg, S., and J. Klymak, 2008: Internal hydraulic jumps and overturning generated by tidal flow over a tall steep ridge. *J. Phys. Oceanogr.*, **38(9)**, 1949-1964.
- Lehner, M., and Coauthors, 2016a: The METCRAX II field experiment: A study of

- downslope windstorm-type flows in Arizona's Meteor Crater. Bull. Amer. Meteor. Soc., 97, 215–235, doi:10.1175/BAMS-D-14-00238.1.
- Lehner, M., R. Rotunno, and C. D. Whiteman, 2016b: Flow regimes over a basin induced by upstream katabatic flows—An idealized modeling study. *J. Atmos. Sci.*, **73**, 3821–3842, doi:10.1175/JAS-D-16-0114.1.
- Li, M., P. Cheng, R. Chant, A. Valle-Levinson, and K. Arnott, 2014: Analysis of vortex dynamics of lateral circulation in a straight tidal estuary. *J. Phys. Oceanogr.*, **44**, 2779–2795, doi:10.1175/JPO-D-13-0212.1.
- Marchesiello, P., J. McWilliams, and A. Shchepetkin, 2001: Open boundary conditions for long-term integration of regional oceanic models. *Ocean Modell.*, **3(1)**, 20, doi: 10.1016/S1463-5003(00)00013-5.
- Martin, W., P. MacCready, and R. Dewey, 2005: Boundary layer forcing of a semidiurnal, cross-channel seiche. *J. Phys. Oceanogr.*, **35**, 1518–1537, doi:10.1175/JPO2778.1.
- Maxworthy, T., 1979: A note on the internal solitary waves produced by tidal flow over a three-dimensional ridge. *J. Geophys. Res.*, **84**, 338–346, doi:10.1029/JC084iC01p00338.
- Mayer, F. T., and O. B. Fringer, 2017: An unambiguous definition of the Froude number for lee waves in the deep ocean. *J. Fluid Mech.*, 831.
- Munk, W., and C. Wunsch, 1998: Abyssal recipes. II: Energetics of tidal and wind mixing. *Deep Sea Res. Part I*, **45**, 1977–2010.
- Nash, J. D., M. H. Alford, and E. Kunze, 2005: Estimating internal wave energy fluxes in the ocean. *J. Atmos. Oceanic Technol.*, **22**, 1551–1570, doi:10.1175/JTECH1784.1.
- New, A.L., K.R., Dyer, and R.E., Lewis, 1986: Predictions of the generation and propagation of internal waves and mixing in a partially stratified estuary. *Estuarine Coastal Mar. Sci.*, **22(2)**, 199-214.
- Peters, H., 1999: Spatial and temporal variability of turbulent mixing in an estuary. *J. Mar. Res.*, **57**, 805–45.
- Pietrzak, J. D., C. Kranenburg, G. Abraham, B. Kranenborg, and A. van der Wekken, 1991:

- Internal wave activity in Rotterdam waterway. J. Hydr. Eng., 117, 738-757.
- Richards, C., D. Bourgault, P. S. Galbraith, A. Hay, and D. E. Kelley, 2013: Measurements of shoaling internal waves and turbulence in an estuary. *J. Geophys. Res.*, **118**, 273–286, doi:10.1029/2012JC008154.
- Rotunno, R., and M. Lehner, 2016: Two-layer stratified flow past a valley. *J. Atmos. Sci.*, **73**, 4065-4076.
- Sarabun C. C., and D. C. Dubbel, 1990: High-resolution thermistor chain observations in the upper Chesapeake Bay. *Johns Hopkins APL Technical Digest*, **11**, 48-53.
- Sturley, D.R. and K.R., Dyer, 1992: A topographically induced internal wave and mixing in the Tamar Estuary. *Dynamics and Exchanges in Estuaries and the Coastal Zone*, D. Prandle, Eds., Vol. 40, *Coastal and Estuarine Studies*, AGU, Washington, D.C., 57-74.
- Vlasenko, V., N. Stashchuk, M. R. Palmer, and M. E. Inall, 2013: Generation of baroclinic tides over an isolated underwater bank. *J. Geophys. Res. Oceans*, **118**, 4395–4408, doi:10.1002/jgrc.20304.
- Wang, D., 2006: Tidally generated internal waves in partially mixed estuaries. *Cont. Shelf Res.*, **26**, 1469–1480, doi:10.1016/j.csr.2006.02.015.
- Warner, J.C., C.R. Sherwood, H.G. Arango, and R.P. Signell, 2005: Performance of four turbulence closure models implemented using a generic length scale method. *Ocean Modeling*, **8**, 81–113.
- Winters, K.B., 2016: The turbulent transition of a supercritical downslope flow: sensitivity to downstream conditions. *J. Fluid Mech.*, **792**, 997–1012
- Xie, X., and M. Li, 2019: Generation of internal lee waves by lateral circulation in a coastal plain estuary. *J. Phys. Oceangr.*, **49**, 1687-1697.
- Xie, X, M. Li, and W. C. Boicourt, 2017a: Breaking of internal solitary waves generated by an estuarine gravity current. *Geophys. Res. Lett.*, **44**, doi:10.1002/2017GL073824.
- Xie, X., M. Li, M. E. Scully, and W. C. Boicourt, 2017b: Generation of internal solitary waves by lateral circulation in a stratified estuary. *J. Phys. Oceangr.*, **49**, 1687-1697,

doi:10.1175/JPO-D-16-0240.1.